Popular Summary for

Radicals and Reservoirs in the GMI Chemistry and Transport Model: Comparison to Measurements

Anne. R. Douglass, Richard S. Stolarski

Atmospheric Chemistry and Dynamics Branch
NASA Goddard Space Flight Center
Greenbelt MD 20771

Susan E. Strahan
Goddard Earth Science & Technology Center
University of Maryland Baltimore Country
Baltimore, MD 21250

Peter S. Connell
University of California Lawrence Livermore National Laboratory
Livermore, CA

The most important use of atmospheric chemistry and transport models is to predict the future composition of the atmosphere. The amounts of gases like chlorofluorcarbons, methyl bromide, nitrous oxide and methane are changing and the stratospheric ozone layer will change because these gases are changing. Methyl bromide, nitrous oxide and methane all have natural sources, and also change because of human activity. Chlorofluorcarbons are man-made gases; these are known to decrease stratospheric ozone and future production is banned. They are long-lived gases, and many decades will pass before they are insignificant in the atmosphere. The models are used to predict changes in ozone and other gases; this is a straightforward application. The models must be also tested using observations for the present day atmosphere. This is a challenging task, because the model contains more than 50 species and more than 150 chemical reactions. Data from satellites, ground stations, aircraft and balloons are used to evaluate the model.

Different models that are used in international assessments produce different results; in the most recent assessment some predict that ozone will return to 1980 levels by 2025 and others predict that this will not happen until 2050. Since all the parts of the models are conceptually the same, there must be differences in implementation that produce these differences. This work takes a single model, two different sets of winds and temperatures, and repeats the same prediction for the future. Here we compare the results for these two simulations with many observations. The purpose is to identify differences in the model results for the present atmosphere that will lead to different predictions. This sort of controlled comparison will reduce uncertainty in the predictions for stratospheric ozone.

Radicals and Reservoirs in the GMI Chemistry and Transport Model: Comparison to Measurements

Anne. R. Douglass, Richard S. Stolarski

Atmospheric Chemistry and Dynamics Branch
NASA Goddard Space Flight Center
Greenbelt MD 20771

Susan E. Strahan
Goddard Earth Science & Technology Center
University of Maryland Baltimore Country
Baltimore, MD 21250

Peter S. Connell
University of California Lawrence Livermore National Laboratory
Livermore, CA

Abstract: We have used a three-dimensional chemistry and transport model (CTM), developed under the Global Modeling Initiative (GMI), to carry out two simulations of the composition of the stratosphere under changing halogen loading for 1995 through 2030. The two simulations differ only in that one uses meteorological fields from a general circulation model while the other uses meteorological fields from a data assimilation system. A single year's winds and temperatures are repeated for each 36-year simulation. We compare results from these two simulations with an extensive collection of data from satellite and ground-based measurements for 1993 - 2000. Comparisons of simulated fields with observations of radical and reservoir species for some of the major ozone-destroying compounds are of similar quality for both simulations. Differences in the upper stratosphere, caused by transport of total reactive

nitrogen and methane, impact the balance among the ozone loss processes and the sensitivity of the two simulations to the change in composition.

1. Introduction

A primary application of atmospheric chemistry and transport models (CTMs) is to assess the impact of human activities on stratospheric ozone through the simulation of changes in natural and anthropogenic trace gases, including chlorofluorocarbons, methyl bromide, nitrous oxide and methane. A useful simulation should minimally produce a calculated present-day atmosphere that compares well with observations. This simple statement carries many implications. The photochemical lifetime of ozone varies over several orders of magnitude, from years in the lower stratosphere to about a day near the stratopause. The relative importance of the various catalytic loss processes that impact ozone varies with altitude, latitude and season. The distributions of reactive radicals and less-reactive reservoir species are affected by the transport of reacting gases and the temperatures at which reactions take place. Testing the many processes and their interaction within the model requires observations of many constituents. Relevant observations may be made from space-based, balloon, aircraft or ground-based platforms.

Two-dimensional (latitude height) simulations of total ozone evolution for past and present atmospheric conditions are similar to observations made since 1979 by Total Ozone Mapping Spectrometers (TOMS) on various satellites as shown in the Scientific Assessment of Ozone Depletion [WMO, 2002, hereafter WMO2002]. Predictions for the future evolution of ozone as chlorofluorocarbons decrease using these same models differ substantially from one another. The conceptual elements of the models (photochemical

mechanism, photolysis scheme, reaction rate data, meteorological fields, numerical transport scheme) are the same, but their implementations differ making it difficult if not impossible to ascertain the reasons that some simulations predict that column ozone will reach 1980 levels by 2025 while others predict that column ozone will not reach that level until after 2050. The Global Modeling Initiative (GMI) is intended to reduce the uncertainty in assessment calculations. The GMI chemistry and transport model (CTM) is three-dimensional, making it possible to improve the physical basis of the assessment through explicit representation of processes that are not resolved in two dimensions. For example, processes important to polar ozone loss are more realistically represented and can be thoroughly evaluated in a 3D framework. The GMI CTM is modular in design so that the sensitivity of the assessment calculation to various CTM components can be quantified. Quantitative comparisons of the simulated present atmosphere with observations make it possible to trace the impact of improvements in CTM components. It may also be possible to attach higher or lower significance to particular assessment results based on CTM performance.

The simulations reported here use the GMI CTM with a stratospheric photochemical mechanism consisting of homogeneous and heterogeneous chemical reactions along with photolytic decomposition. The mechanism represents more than 70 years of research since the first chemical mechanism with only oxygen reactions proposed by *Chapman* [1930]. In the late 1960s and early 1970s catalytic reactions of hydrogen, nitrogen, chlorine, and bromine oxides were recognized and introduced into the mechanism. In the mid-1980s, after the discovery of the ozone hole, heterogeneous reactions on the surfaces of sulfate aerosols and polar stratospheric clouds (PSCs) were

recognized and are now part of the mechanism. This evolving mechanism has been tested against many detailed atmospheric measurements of the source gases, reservoirs and radicals. Here we present 3D simulations using this basic mechanism with two representations of the dynamics of the atmosphere. Results illustrate how simulated constituent distributions are produced through interaction of the chemical mechanism with transport.

These two GMI CTM simulations of the period 1995 – 2030 are identical in all respects except the input meteorological fields. One set of fields is taken from a general circulation model (GCM) that was developed through a collaboration of NASA with the National Center for Atmospheric Research (NCAR). This Finite Volume GCM (FVGCM) uses a flux-form semi-Lagrangian transport scheme [*Lin and Rood,* 1996, 1997] and a quasi-Lagrangian vertical coordinate system [*Lin,* 1997] to ensure accurate representation of transport by the resolved-scale flow. The FVGCM has horizontal resolution 2° latitude by 2.5° longitude and extends from the surface to 0.01 hPa. Physical parameterizations in this version of FVGCM are from version 3 of the NCAR Community Climate Model (CCM3) described by *Kiehl et al.* [1998]. The second set of fields is taken from a version of the Goddard Earth Observing System Data Assimilation System that uses the FVGCM at its core (the Finite Volume Data Assimilation System FVDAS).

Schoeberl et al. [2003] and *Douglass et al.* [2003] use trajectories and a CTM respectively to show that tropical transport calculated using winds from FVGCM is more realistic than that calculated using winds from FVDAS. *Strahan and Douglass* [2004] (hereafter refereed to as SD2004) evaluated transport characteristics of the GMI CTM for

these two sets of meteorological fields. SD2004 show that tracer distributions produced by GMI_{FVGCM} (the GMI CTM when driven by winds from FVGCM) are more similar to observed distributions than those produced by GMI_{FVDAS} (the GMI CTM driven by winds from FVDAS) at middle and high latitudes. Consistent with that, GMI_{FVGCM} mean age in the polar lower stratosphere is older (more realistic) that that of GMI_{FVDAS} [*Considine et al.*, 2004]. Overall, the GMI_{FVGCM} constituent distributions compare best with observations in the middle stratosphere, and are more similar to observations in the northern hemisphere than in the southern hemisphere. GMI_{FVDAS} distributions are more realistic than those from GMI_{FVGCM} only in the southern hemisphere upper stratosphere during spring and fall. The greatest southern hemisphere wave activity occurs during this period [*Randel*, 1988], and the good comparisons for GMI_{FVDAS} are consistent with a more realistic representation of planetary waves through the combination of the FVGCM with observations in the assimilation system. The tropical transport barrier is well represented by GMI_{FVGCM} but not by GMI_{FVDAS}. The polar transport barrier is better represented by GMI_{FVGCM} than GMI_{FVDAS}, but neither simulation maintains a realistic vortex edge.

Here we focus on aspects of GMI CTM performance related to the photochemical mechanism (section 2) using comparisons of calculated distributions of reservoir and radical species with observations (section 3). The relative importance of the primary loss processes for ozone in the two simulations is discussed in section 4. A discussion and summary are given in section 5. The differences in input meteorological fields are shown to lead to differences in the relative importance of the ozone loss processes involving chlorine and nitrogen species, thus transport differences presented in SD2004 and

comparisons of the reservoir and radical species with observations shown here have implications for the assessment calculation.

2. Model description and assessment scenarios

a. The GMI chemistry and transport model

The GMI CTM used in this study is an improved version of that described by *Douglass et al.* [1999], *Considine et al.* [2000], and *Rotman et al.* [2001]. That version was applied to characterization of the effects of high-speed civil aircraft [*Kinnison et al.*, 2001]. The constituent continuity equations are operator-split and 2-D domain-decomposed in the horizontal dimensions for execution on parallel computers. The split operator cycles through advective, photochemical and physical processes such as tropospheric deposition and rainout. The overall time step of one hour is stable, maintains an acceptable level of accuracy, and advances the simulation rapidly enough to be practical.

The flux form semi-Lagrangian numerical transport scheme [*Lin and Rood*, 1996] has been modified to enforce conservation of mass when the surface pressure field changes at the 6 hourly meteorological update times [*Prather et al.*, 1987]. The unmodified advection algorithm conserves mass if the divergence calculated from the input wind fields is consistent with the time trend of the surface pressure field. The mass increases when these are inconsistent as for meteorological fields from a data assimilation system. In such a system data insertion to produce the analysis fields (used in the CTM) modifies the surface pressure of the forecast field. For meteorological fields from a GCM, a smaller inconsistency may arise because winds are input to the CTM at 6-hour

intervals, a much longer time-step than used in the GCM [*Jöckel et al.*, 2001]. Horizontal mass fluxes are adjusted to conserve tracer mass across updates to the wind fields [*Prather et al.*, 1987]. Vertical mass fluxes are unchanged. After adjustment total mass is conserved for constituents without losses such as SF_6. Species profiles are altered near sharp gradients, e.g., the upper tropospheric ozone profile. The horizontal adjustment has little impact on horizontal species distributions.

Individual species are advected separately, with the exception of atomic radicals. Early test runs using meteorological fields from a data assimilation system showed unrealistic horizontal structure, including spurious stratospheric maxima in the distributions of total inorganic chlorine and bromine. This problem was obvious because the maxima exceeded the sum of halogens available from the source gases. Although the advection algorithm conserves mass, it is dispersive when the photochemical operator produces steep spatial gradients at the day/night terminator. The net effect of this dispersion is to produce non-physical maxima. Since this dispersion is minimal in the absence of steep gradients, total inorganic chlorine or bromine can be transported without this error. The spurious maxima are eliminated by advecting total inorganic chlorine (or bromine), in addition to advection of the individual members, and using this result to scale each member of the group. At the beginning of each time step the SMVGEAR II solver [*Jacobsen,* 1998] adjusts the partitioning among the inorganic halogens. A complication arises when a species (e.g., BrCl) is a member of both groups. In such cases, we adjust the chlorine group to account for any change in partitioning of the species in the bromine group since the chlorine abundance is substantially larger.

The GMI aircraft assessment calculations employed the Onera-SIS semi-implicit photochemistry solver [*Kinnison et al.*, 2001]. The more accurate but slower SMVGEAR II solver was also implemented in the GMI CTM and was used to benchmark other solvers [*Rotman et al.*, 2001]. Performance has been increased through implementation of interactive, on-the-fly, calculation of the grid cell error tolerances applied in the algorithm, based on the local distribution of species abundances as described by *Jacobson* [1998], making it practical to use SMVGEAR II for these simulations. Fifty-two chemically active species are included in the mechanism. Kinetic input for this mechanism, which includes 122 thermal reactions and 44 photolytic processes, is taken from *Jet Propulsion Laboratory Evaluation 13* [*JPL,* 2000] (hereafter referred to as JPL2000) with the exception of the reactions of HCFC reactions, which come from JPL2003. Updates to the *Rotman et al.* [2001] mechanism include the addition of chlorine source gases HCFC-141b (CH_3CFCl_2) and HCFC-142b (CH_3CF_2Cl) and the bromine source gases Halons-1202 (CF_2Br_2) and -2402 (CF_2BrCF_2Br) specified in future scenario A2 by WMO2002 (which also used JPL2000).

The source gases are held to surface mole fraction boundary conditions, which are effectively propagated upward by rapid tropospheric transport, thus the HCFC mixing ratios at the tropical tropopause are nearly equal in the two simulations.

Considine et al. [2000] developed the parameterization for the effects of polar stratospheric clouds. The heterogeneous reactions of gases on the cloud particle surfaces are treated as pseudo-first-order (e.g. N_2O_5 + liquid binary sulfate aerosol = HNO_3) or pseudo-second-order (e.g. $ClONO_2 + HCl + NAT = Cl_2 + HNO_3$). *Considine et al.* [2004] discuss polar processes in the two simulations in detail.

b. Ozone recovery scenarios

The input meteorological fields from FVGCM and FVDAS were intentionally selected to have a cold Arctic winter to examine a 'worst-case scenario' for ozone recovery. The FVDAS winter of 1999-2000 was selected because the winter Arctic vortex lasted into the spring with abundant PSCs and significant ozone loss [*Newman et al*, 2002]. The selected year of FVGCM meteorology closely matches these criteria. SD2004 compare polar temperature behavior in these model years. The FVGCM and FVDAS Arctic temperatures were climatologically near normal except that March was colder than usual. The FVGCM on average was a little warmer than the FVDAS and will produce smaller areal and temporal PSC coverage. The model year begins July 1 and ends June 30 because this is the period with lowest overall planetary wave activity and with low interannual variability in wind fields [*Randel,* 1988], thus this choice minimizes adjustments to the circulation caused by recycling one year of winds.

The initial condition for these simulations is taken from a seven-year integration using source gas surface boundary conditions for 1995 and is close to a periodic 'steady-state'. Relevant observations are compared with simulated fields for 1995. During the 36-year integrations projected changes in source gas boundary conditions follow those of Scenario A2 of WMO2002 and are updated monthly. During 1995-2000 the simulations make a transition from the periodic 'steady-state' stratosphere to a state representing the transient burdens given the trends in boundary conditions and the characteristic mixing times of the meteorological fields.

The surface area density of liquid binary sulfate stratospheric aerosol input to the GMI CTM, specified for Scenario A2, is based on observations from 1995 through 1999. The 1997 "clean atmosphere" distribution is used for years 2000-2030.

3. Comparisons with Observations

The following comparisons with observations illustrate the effects of transport on partitioning of constituents and on the balance among the loss processes affecting ozone. These comparisons are essential to determine whether the response of simulated ozone to the prescribed change in chlorine source gases is realistic in either simulation.

a. Chlorine species

Chlorine-catalyzed ozone destruction depends on the total inorganic chlorine (Cl_y) and the partitioning between the radical chlorine monoxide (ClO) and reservoir gases hydrochloric acid (HCl) and chlorine nitrate ($ClONO_2$). Transport differences between the two simulations produce differences in the distributions of total inorganic chlorine as well as in the distributions of NO_y, CH_4 and O_3, all of which affect chlorine partitioning. We use observations from many instruments to evaluate model performance for chlorine species. These include HCl profiles from the Halogen Occultation Experiment (HALOE) [*Russell et al.,* 1993] on the Upper Atmosphere Research Satellite (UARS), $ClONO_2$ profiles from the Cryogenic Limb Array Etalon Spectrometer (CLAES) [*Roche et al.,* 1993] on UARS, ClO profiles from the Microwave Limb Sounder (MLS) [*Barath et al.,* 1993; *Waters et al.,* 1996; *Livesey et al.,* 2003] also on UARS, MkIV profiles of Cl_y obtained by combining measurements of individual chlorine species [*Toon,* 1991] and column observations of HCl from Network for Detection of Stratospheric Change

(NDSC) sites. The NDSC measurements of HCl and HNO_3 are publicly available at http://www.ndsc.ncep.noaa.gov. The measurements at some of the sites are described in more detail by *Koike et al.*, [1994], *Schneider et al.*, [2003], *Rinsland et al.* [2003a; 2003b]. UARS data are available from the Goddard Distributed Active Archive Center http://daac.gsfc.nasa.gov .

The seasonal variation of the differences $Cl_y(GMI_{FVGCM})$– $Cly(GMI_{FVDAS})$ shown for 50°S and 50°N (Figure 1a and 1b) is consistent with the SD2004 transport evaluation. Cl_y differences are less than 5% above 10 hPa for most of the year at both latitudes because the A2 scenario prescribes mixing ratio boundary conditions for all source gases that contribute to stratospheric inorganic chlorine. Lower stratospheric Cl_y from GMI_{FVGCM} is greater than that from GMI_{FVDAS} (0.35 ppmv (18%) and 0.79 ppmv (35%) at 31 hPa in the northern and southern hemispheres respectively), reflecting the slower circulation and older age-of-air for the FVGCM meteorological fields.

Figure 2 compares simulated Cl_y profiles with estimates from observations. One estimate is obtained by summing the different species comprising Cl_y profiles measured by the MkIV instrument at 30°N in September 1996 and 70°N March 2003 [*Toon*, 1991]. A second Cl_y estimate is obtained using trajectories to combine non-coincident HALOE HCl and CLAES $ClONO_2$ [*Dessler et al.*, 1995]. At 70°N, the lower bound of Cl_y from GMI_{FVGCM} matches the upper bound of Cly from GMI_{FVDAS} between 400 and 800K. The MkIV profiles fall within one standard deviation of the CLAES + HALOE estimate. The systematic error for the CLAES + HALOE Cl_y, estimated to be 30%, is not shown. At 30°N the GMI_{FVGCM} Cl_y falls within the CLAES + HALOE estimate at 550K and 650K; here GMI_{FVDAS} Cl_y falls below. The MkIV Cl_y is higher than the CLAES + HALOE

estimate above 650K. In the southern hemisphere, where the simulations differ the most, the GMI_{FVGCM} Cl_y falls within the CLAES + HALOE estimate at 550K and 650K, whereas the GMI_{FVDAS} Cl_y is too low. At 800K the GMI_{FVGCM} profile is near the upper bound of observations; the GMI_{FVDAS} profile is near the lower limit. Overall, Cly from GMI_{FVGCM} is closer to observations than that from GMI_{FVDAS}.

The simulated HCl columns depend on the partitioning between HCl and $ClONO_2$ as well as the total Cly. The fraction HCl/Cly is slightly greater in GMI_{FVGCM} in the lower stratosphere, resulting from the inverse dependence of HCl/Cly on the ozone mixing ratio and the somewhat smaller ozone mixing ratios in the GMI_{FVGCM} lower stratosphere as shown below. Figure 3 compares daily values of column HCl between 100 hPa and 1 hPa calculated from HALOE profiles for latitudes 40°S-50°S and 40°N-50°N for 1993 – 2000 with simulated zonal average columns at 46°S and 46°N. The NH (SH) column HCl from GMI_{FVGCM} is ~8% (~16%) larger than that from GMI_{FVDAS} as Cl_y and HCl/Cl_y are greater in GMI_{FVGCM} than in GMI_{FVDAS}. Both time series fall within the envelope of observations, however HALOE HCl profiles fall below correlative profiles used in validation of the HALOE measurements, and the HALOE columns may underestimate the actual columns by about 10% [*Russell et al.*, 1996]. The columns from GMI_{FVDAS} are at the lower edge of the envelope in the southern hemisphere. Overall these column comparisons are consistent with the Cl_y profile comparisons, and show that Cl_y in GMI_{FVGCM} is more realistic. Neither HALOE nor the simulations exhibit a clear seasonal cycle in the column above 100 hPa.

Daily FTIR measurements for several years at four NDSC stations are compared to the simulated columns for 1995 in Figure 4. At Jungfraujoch (Figure 4a), there is a

late spring maximum of 4-5x10^{15}cm^{-2} and a summer minimum of 3.5-4.2x10^{15}cm^{-2}. Seasonal behavior from both simulations is consistent with that observed. The HCl columns from GMI_{FVGCM} are 13% smaller than the observed mean, while those from GMI_{FVDAS} are smaller by 20%. At Izana (28.3°N, Figure 1b) and Mauna Loa (19.5°N, Figure 1c) both simulations agree well with the data. In the southern mid-latitudes at Lauder (45°S, Figure 1d), the magnitude and seasonal cycle of GMI_{FVGCM} columns agree with observations. The GMI_{FVDAS} columns are smaller than the observed columns and poorly represent the seasonal cycle observed at Lauder.

The simulations provide insight into the origin of the northern midlatitude seasonal cycle that is apparent in the ground-based columns but absent from the HALOE column for 100hPa – 1 hPa. The seasonal cycles of the partial pressure of HCl for GMI_{FVGCM} and GMI_{FVDAS} (Figure 5) show that changes in composition in the lowermost stratosphere (below the lower limit of the HALOE column) contribute most to the seasonal cycle. This seasonal dependence, produced by isentropic transport of upper tropical tropospheric air into the lowermost stratosphere during summer, is consistent with that observed for ozone [*Rood et al.*, 2000], chlorofluorcarbons [*Ray et al.*, 1999] and water vapor [*Gettelman et al.*, 2000; *Pan et al.*, 2000]. The comparison suggests that the seasonal dependence of the mix of air of stratospheric and tropospheric origin in the lowermost stratosphere is appropriately represented in GMI_{FVGCM}.

Although Cl_y above 10 hPa is nearly identical in the two simulations, small differences in the fraction HCl/Cl_y have a significant impact on the ClO mixing ratio. MLS ClO profiles, retrieved with the V5 algorithm [*Livesey et al.*, 2003], are compared with simulated profiles to test the realism of the profile shape, daytime maximum, and

diel variation. Four years of MLS observations are sorted according latitude and zenith angle to determine annual average daytime and nighttime profiles for twenty-degree latitude bands centered on 45°S, 45°N, and the equator. Precision uncertainties in these profiles are negligible due to the large number of profiles averaged. The simulated annual average daytime and nighttime ClO profiles are compared with the MLS averages in Figure 6.

The MLS daytime ClO peak mixing ratio is near 3 hPa in both the tropics and middle latitudes; the MLS middle latitude peak mixing ratio is 0.2 ppbv greater than that in the tropics. The MLS nighttime profile peak is near 2 hPa; this is expected because nighttime $ClONO_2$ formation is less important at lower pressure. Below about 6 hPa the nighttime MLS measurement is unrealistically high; these mixing ratios of ~0.1 ppbv are recognized as a bias in the measurement [*Livesey et al.*, 2003]. This bias, significant at pressures higher than ~6 hPa, is also present in the daytime measurement and is eliminated by computing difference profiles as shown in the right hand column. At middle latitudes the daytime and nighttime ClO and the day-night ClO differences simulated by GMI_{FVDAS} are close to MLS values; all three peak mixing ratios simulated using GMI_{FVGCM} exceed observations. The peak day-night difference in the GMI_{FVGCM} ClO simulation is about 0.2 ppbv greater than MLS; which exceeds the MLS systematic measurement error (~0.1 ppbv at the peak). In the tropics the simulations agree with each other, but both show higher peak mixing ratios for daytime ClO and larger than observed day-night differences. These differences also are larger than the estimated systematic error for MLS ClO.

Since Cl_y is the same in the two simulations, the difference in ClO between the two simulations is due to differences in partitioning among chlorine species. HCl is ~75% of total Cly at middle latitudes near 2-3 hPa; small differences in the fraction HCl/Cly leads to differences in the fraction ClO/Cl_y. In the tropics at 3.2 hPa, where ClO/Cly is less than 0.05 throughout the year, the ratio is smaller in GMI_{FVGCM} than in GMI_{FVDAS}. Poleward of 30° latitude the ratio is 0.05 – 0.2 throughout the year (except during polar night) and the fraction ClO/Cl_y is 20-40% larger in GMI_{FVGCM} than in GMI_{FVDAS} at these latitudes, due to reduced formation of HCl through reaction of Cl with CH_4. SD2004 show that the most probable value of CH_4 from GMI_{FVGCM} in the middle latitude upper stratosphere is lower than indicated by Cryogenic Limb Array Etalon Spectrometer (CLAES) measurements [*Roche et al.*, 1993], whereas that from GMI_{FVDAS} is closer to the observations. Chlorine-catalyzed ozone loss is more important in the present day atmosphere produced by GMI_{FVGCM} than in the GMI_{FVDAS} as will be discussed further in section 4.

Below about 4 hPa, ClO is converted to $ClONO_2$ during the night, and their sum is approximately constant for periods of minimal change in species such as O_3 and CH_4 that impact partitioning between the reservoirs [e.g., *Dessler et al.*, 1995]. Comparisons of the observations with simulation results for the diel variation of CLAES $ClONO_2$ [*Mergenthaler et al.*, 1996] complement the comparisons with MLS ClO. Observations made between September 21 and October 29, 1992 between 40°N and 50°N are compared to the two simulations at 10 hPa and 4.6 hPa in Figure 8. The observed day-night difference in $ClONO_2$ at 10 hPa is in good agreement with the day-night variation in ClO (Figure 6) and in good agreement with observations. At 4.6 hPa simulated $ClONO_2$

exceeds observations both day and night, although the day-night difference is close to that observed for GMI_{FVDAS}. A second aspect of comparison is the shape of the diel signal. The timing of the sunrise decrease in $ClONO_2$ matches that observed at both pressures. The simulated sunset rise matches observations at 10 hPa but at 4.6 hPa the model increase begins sooner and takes place more rapidly than that observed by CLAES. The daytime value of $ClONO_2$, a balance between destruction through photolysis and the three-body formation reaction of NO_2 with ClO, is nearly the same in both simulations due to compensating differences in NO_2 and ClO, and exceeds that observed. These discrepancies suggest that formation of $ClONO_2$ is slower than modeled at 4.6 hPa.

The key points from comparisons with chlorine species are the following: 1) Cl_y from GMI_{FVGCM} is greater than that from GMI_{FVDAS} outside the tropics; 2) limited comparisons with observational values for Cl_y support the higher Cl_y in GMI_{FVGCM}; 3) comparisons of the HCl column with ground-based observations in both hemispheres favor GMI_{FVGCM} due to its higher Cl_y; 4) there are small differences in partitioning between HCl and $ClONO_2$ that are inconsequential in much of the stratosphere ; and 5) comparisons of ClO in the upper stratosphere favor GMI_{FVDAS}. The small difference in the fraction HCl/Cly in the upper stratosphere leads to a significant difference in upper stratospheric ClO, with lower HCl and higher ClO in GMI_{FVGCM} as a result of lower CH_4. This will be discussed in section 4.

b. Reactive Nitrogen ($NO_y = HNO_3 + NO + NO_2 + NO_3 + 2*N_2O_5 + HO_2NO_2$)

Most N_2O in the stratosphere is destroyed through photolytic decomposition to N_2+O. Total reactive nitrogen (NO_y) is produced through a much smaller N_2O loss process,

reaction with $O(^1D)$, and lost through the reaction of N + NO. Maximum production takes place in the tropics at about 15 hPa; maximum loss also takes place in the tropics, but at a higher altitude than maximum production. Soluble species such as HNO_3 are removed by rainout in the troposphere. Observations used to evaluate model performance for reactive nitrogen species include NO_y, the sum of the individual species measured by MkIV [*Toon et al.*, 1991; *Sen et al.*, 1998], measurements of NO_y [*Fahey et al.*, 1989] made from the ER-2 during the second Airborne Arctic Stratosphere Expedition [*Wofsy et al.*, 1994], sunset profiles of HALOE NO and NO_2 [*Gordley et al.*, 1996], retrieved using algorithm Version 19, and NSDC columns of HNO_3 [*Koike et al.*, 1994].

In the lower stratosphere, where transport and mixing are rapid compared to photochemical processes, N_2O and NO_y should show close correlation [*Plumb and Ko*, 1992]. The slope of the correlation changes higher in the stratosphere, where the chemical loss of NO_y is important. Figure 9 compares the zonal mean mixing ratios of NO_y as a function of N_2O at 34°N for the two GMI simulations with MkIV measurements at 35°N in September 1993 [*Toon*, 1991; *Sen et al.*, 1998]. Additional observations from the ER2 aircraft gathered between 25°N and 35°N during February 1992 are also included. Both simulations are similar to observations where N_2O levels are above 100 ppbv and N_2O and NO_y are controlled by transport and the implied branching ratio for NO_y production. Higher in the stratosphere both simulations show the roll-off in NO_y consistent with MkIV observations. This comparison was used as a metric of model performance for evaluation of the effects of high-speed aircraft on stratospheric ozone (see Figure 4.2 in *Kawa et al.* [1999]). The simulated NO_y peak mixing ratios are around 1 ppbv below the observations for GMI_{FVGCM} and close to 2 ppbv below observations for

GMI_{FVDAS}. This comparison shows that simulated NO_y and N_2O are related as observed away from the production and loss regions. Differences in observed and modeled N_2O will be echoed by differences in NO_y; the zonal mean distributions from the two simulations in Figure 9(b) show large differences due to the more vigorous residual circulation and horizontal outflow above 10 hPa from the tropics in GMI_{FVDAS}. Below 10 hPa and below the NO_y peak, less horizontal outflow leads to higher middle latitude NO_y in GMI_{FVGCM}. Above 10 hPa this lack of horizontal transport leads to lower NO_y in GMI_{FVGCM} and lower CH_4 than observations as discussed by SD2004.

Figure 9(b) shows much higher NO_y in the middle stratosphere in GMI_{FVGCM} than in GMI_{FVDAS}. The ground-based column observations HNO_3 (Figure 10) are used to discriminate between the simulations since HNO_3 is more than 50% of total NO_y below 20 hPa and is more than 50% of the column NO_y outside the tropics. Except at Mauna Loa, the simulated columns GMI_{FVGCM} are near the lower edge of the measurement range; simulated columns from GMI_{FVDAS} fall below that range. The observed maximum to minimum difference is about 8 $x10^{15}$cm-2 (close to 50% of the winter maximum) in both hemispheres; the simulated maximum to minimum difference is 40% for GMI_{FVGCM} and 37% for GMI_{FVDAS}. For HNO_3, both transport in the lowermost stratosphere and summer photochemical loss throughout the stratosphere contribute to the seasonal cycle. These comparisons suggest that lower stratospheric NO_y is unrealistically low in the GMI_{FVDAS} simulation. A more recent recommendation [*JPL*, 2003] for the gas-phase formation of HNO_3 through combination of the hydoxyl radical (OH) with nitrogen dioxide (NO_2) would reduce formation of HNO_3 and lead to higher NO_x in the middle stratosphere. The difference in NO_x as a percentage of NO_y can be as large as 25% during winter at high

latitudes at 10 hPa. This would worsen the column comparison only slightly since the lower stratosphere makes a much larger contribution to the HNO_3 column; the sense of this change is opposite to that required to improve the representation of the seasonal cycle.

This underestimate of the HNO_3 columns is not unexpected. The lower right panel of Figure 4 of SD2004 shows a summer northern hemisphere comparison of N_2O from GMI_{FVGCM} and GMI_{FVDAS} with a climatology developed from ER2 data [*Strahan et al.*, 1999]. Both simulations show greater than observed N_2O. Similarly, profiles of NO_y for the two simulations show low NO_y compared to ER2-derived NO_y [*Strahan,* 1999] for June at 45°N (Figure 11).

Above 10 hPa, $NO_x = NO + NO_2 + 2 * N_2O_5$ comprises more than 70% of NO_y, which we evaluate using HALOE profiles of NO and NO_2. The simplest way to compare HALOE NO and NO_2 [*Gordley et al.,* 1996] with the simulation results is to compare the observed sum $NO + NO_2$ at sunset with model $NO_x = NO + NO_2 + 2*N_2O_5$ at any time of day, noting that N_2O_5 is negligible at sunset [*Kumer et al.,* 1997]. Sunset data for 1993 – 2000 for 3.2 hPa and 6.8 hPa are compared with simulated values for NO_x in Figures 12 and 13. The boundaries of the shaded area are the mean ± 1 standard deviation of all observations within 10 degrees of the specified latitude. In the tropics both simulations fall within the band defined by the observations at 3.2 hPa. At northern middle latitudes, both fall within the band defined by observations for most of the year. At southern middle latitudes, the NO_x from GMI_{FVGCM} is below the band defined by observations most of the year. Neither simulation exhibits a clear seasonal cycle, yet such a cycle is obvious at the middle latitudes shown. The difference between the maximum and

minimum mixing ratios is ~8 ppbv in the northern hemisphere and ~11 ppbv in the southern hemisphere. Neither simulation suggests a seasonal-cycle amplitude of more than 2 ppbv. Outside the tropics, NO_x from GMI_{FVGCM} is lower than that from GMI_{FVDAS} by as much as 4 ppbv (~25%).

At 6.8 hPa, the simulations are more similar to each other than at 3.2 hPa. NO_x from both simulations is significantly lower than observations in the tropics and southern middle latitudes; in the northern hemisphere middle latitudes the simulations agree with each other and with observations.

c. Ozone

The mixing ratio of ozone at any latitude and altitude may vary due to transport of ozone or transport of constituents affecting ozone. Temperature affects the ozone mixing ratio through temperature dependent photochemical processes. Both of these vary seasonally. Here we use probability distribution functions (PDFs) [*Sparling*, 2000] calculated from HALOE observations to evaluate the simulated ozone fields [*Strahan*, 2002]. The HALOE observing pattern sweeps through latitude so that near global coverage is provided each month; HALOE has made observations since fall 1991, and combination of observations from 1993-2000 within a specified month and season meets the requirement that the shape of a histogram of observations does not change when subsets of observations are randomly omitted. Vertical resolution fc one profiles is about 2 km; the ozone mixing ratio error estimates for version 17 are ~10% between 50 hPa and 1 hPa, and ~30% at 100 hPa [*Brühl et al.*, 1996]. The ozone profiles used here are retrieved using algorithm version 19 and are nearly identical to the version 17 profiles in the region of interest. Contours of the temporal evolution of PDFs show the evolution

of the most probable value and its variability [*Sparling*, 2000]. Column ozone measurements from the Total Ozone Mapping Spectrometer (TOMS) instrument on the Earth Probe satellite are also used to evaluate CTM performance. These data are processed with the TOMS algorithm version 7 [*McPeters et al.*, 1998].

Seasonal cycles of HALOE PDF's are compared with those from GMI_{FVGCM} and GMI_{FVDAS} for 46 hPa, 10 hPa and 2.15 hPa for 10-degree latitude bands centered on 45°S, the equator, and 45°N (Figure 14 a-c). In spite of transport differences discussed by SD2004 and the radical and reservoir differences described above, the PDFs from the two simulations are similar to each other. At 2 hPa, the seasonal minima at middle latitudes (Figure 14(a) and Figure14(c)) occur in summer. During winter the distributions are broader due to planetary wave activity that contributes to ozone variability through transport and through temperature variations affecting temperature dependent loss processes. The most probable value for ozone in the summer is smaller than observed for both simulations. The difference between the most probable values in the winter and summer from HALOE is close to that from GMI_{FVGCM} and smaller than that from GMI_{FVDAS}. In the tropics (Figure 14(b)), all distributions exhibit a semi-annual cycle, but the observed most probable value for ozone is 0.6 - 1 ppmv (10 - 25%) greater than that of either simulated distribution. The observed distribution is broadest of the three. The distribution from GMI_{FVGCM} is more strongly peaked than that from GMI_{FVDAS}.

At 10 hPa the observed and simulated midlatitude PDFs (Figure 14(a) and 14(c)) are similar even though the winter planetary wave activity is greater in GMI_{FVDAS} than GMI_{FVGCM} based on comparisons of observed and simulated CH_4 as shown in SD2004. Middle stratospheric ozone is less sensitive to transport than tracers such as CH_4 as

shown by *Douglass et al.* [1997] for a simulation driven by winds from an earlier version of the data assimilation system. The summer distribution from GMI_{FVGCM} is more sharply peaked than that calculated from the HALOE observations or from the GMI_{FVDAS}. In the tropics (Figure 14(b)), the distribution derived from HALOE is influenced by the quasi-biennial oscillation [e.g., *Randel et al.*, 1997; *Gray and Russell*, 1996] and is broader than the simulated distributions. Both simulations recycle a single year's winds leading to less variability than observed.

In the lower stratosphere there are more differences than similarities between the observed and simulated probability distributions for ozone. In the tropics (Figure 14(b)), the HALOE distribution is nearly constant. The distribution is peaked with 70% of the observations within 15% of the most probable value throughout the year. The distribution from GMI_{FVGCM} exhibits similar variability during May-September, but the amplitude of the annual cycle is much greater than observed and the variability is seasonally dependent. The variability produced by GMI_{FVDAS} is much greater than observed throughout the year. Fewer than 60% of the simulation values are within 15% of the most probable value during most of the year, and for some months fewer than 40% of the simulation values meet this criteria. This excess variability is a signature of the difficulty of producing physically consistent meteorological fields in the tropics through combination of a general circulation model (GCM) forecast with observations of temperature and winds in the assimilation process. Tropical winds are not related strongly to the temperature as in middle and high latitudes, and there is bias between the GCM forecast and the temperature data. These issues are discussed in detail by *Schoeberl et al.* [2003] and by *Douglass et al.* [2003].

At middle latitudes (Figures 14(a) and 14(c)), the most probable value for HALOE measurements at 46 hPa exhibits an annual variation of about 2 ppmv with a summer minimum in both the most probable value and the variability. The seasonal dependence of the variability of the GMI_{FVGCM} distribution is similar to that observed in both hemispheres, but the most probable value varies by only about 1 ppmv. The most probable value from GMI_{FVDAS} varies by less than 0.5 ppmv, and the distribution is broad throughout the year. The summertime decrease in ozone and accompanying decrease in variability occurs because photochemical loss dominates the ozone tendency during the summer at middle and high latitudes [*Newman et al.*, 1999; *Brühl and Crutzen*, 2000]. Neither simulation replicates the rapid decrease seen in HALOE ozone between April and June at 46 hPa. The JPL2000 recommendation for formation of HNO_3 leading to lower NO_x than would be computed using JPL2003 may contribute to this discrepancy.

Comparison of TOMS with simulated column ozone is a standard test of model realism, as the model total ozone is sensitive to the lower stratospheric circulation [e.g., *Jackman et al.*, 1991]. Figure 15(a) shows the daily 1994-98 averages of the zonal mean total ozone observed by TOMS between 60°S and 60°N. Figures 15(b) and 15(c) show the differences between TOMS and simulated column ozone for GMI_{FVGCM} and GMI_{FVDAS} respectively. The total ozone from GMI_{FVGCM} is smaller than TOMS in the tropics and middle latitudes. In GMI_{FVDAS} the total ozone is ~ 25 DU less than TOMS in the tropics but higher for much of the year at middle latitudes. This reflects the overly vigorous residual circulation found in the assimilated wind fields. Note that both comparisons would be improved in the tropics if the simulations included photochemical production of tropospheric ozone. Although the model circulations for GMI_{FVGCM} and GMI_{FVDAS} are

quite different, and the biases shown in Figure 15(b) and 15(c) are of different character, the overall comparisons are of similar quality. The simulated annual average total ozone between 60°S and 60°N differs from TOMS by less than 3%, with the GMI_{FVDAS} producing more ozone than observed and GMI_{FVGCM} producing less. The column ozone comparison may suggest particularly unrealistic stratospheric circulations, however, the comparisons here and in SD2004 show that simulations can have large differences in tracer fields and the balance of ozone loss processes while at the same time producing "realistic" total ozone. The comparisons with constituents other than ozone (CH_4, NO_x, NO_y, ClO, HCl) provide information about the realism of the simulation that cannot be obtained from comparisons of just total ozone or profile ozone with observations.

4. Relative Importance of Loss processes

The comparisons of ozone with HALOE observations presented in the previous section are similar for the two simulations. The differences between the simulated columns and TOMS observations (e.g., lower column ozone in the tropics in GMI_{FVGCM} compared with GMI_{FVDAS}) are consistent with differences in the circulation, i.e., tropical upwelling in GMI_{FVDAS} is stronger than in GMI_{FVGCM}. SD2004 note discrepancies with tracer observations throughout the lower stratosphere that are due to the too strong upwelling in GMI_{FVDAS} and too much horizontal transport. Lower stratospheric N_2O is too high, Cly is too low, and the age of air is too young for GMI_{FVDAS}. The comparisons with radical species show important differences between simulations and observations for both sets of meteorological fields, thus it is relevant to compare the photochemical processes in each simulation to understand how they contribute to the present-day ozone distribution.

The loss described below was calculated off line using rate-limiting processes. Losses due to polar processes such those involving the ClO dimer are not included. The total loss is nearly the same in the two simulations, and is shown for 46 hPa and for 3.2 hPa in Figure 16. The 3.2 hPa level is shown because the peak ClO and the greatest ClO difference in the two simulations are found at this level. The difference in the integrated annual loss is less than 6% outside the tropics. This is not surprising because the total loss is nearly equal to the production by photolysis of O_2 that is nominally the same in the two simulations. Transport differences do not affect the total loss but they do affect fraction of total loss due to reactions involving nitrogen, chlorine, hydrogen and oxygen species. These fractions are given in Figure 17 for GMI_{FVGCM} and Figure 18 for GMI_{FVDAS}. There are obvious differences in the importance of the NO_x and Cl_x ozone loss processes. Outside the tropics, reactions involving chlorine radicals account for ~10% more of the total loss for GMI_{FVGCM} compared with GMI_{FVDAS}. Reactions involving nitrogen radicals account for ~10% less of the total loss. The loss due to reactions involving hydrogen radicals and the loss due to reaction of $O + O_3$ are similar in magnitude, and the same annual cycles are apparent in both simulations.

The total loss from GMI_{FVDAS} is similar to that from GMI_{FVGCM} at 46 hPa. The loss increases at high latitude during the summer in both simulations [*Newman et al.*, 1999]. The fractions attributed to the four different families of species are nearly identical in the two simulations (not shown), and reactions involving the nitrogen family account for the somewhat higher summer loss in GMI_{FVGM} than in GMI_{FVDAS}. The NO_y from GMI_{FVGCM} is closer to the ER2 NO_y climatology than that from GMI_{FVDAS}, although a significant difference remains (Figure 11); the somewhat larger loss is consistent with slightly better

agreement of GMI_{FVGCM} ozone with HALOE (Figure 14(a)). In addition to the low bias in NO_y, the smaller than observed seasonal cycle of the middle latitude HNO_3 column (Figure 10) points towards a common deficiency in the summer production of nitrogen radicals from the HNO_3 reservoir that could account for the weaker than observed seasonal cycle in ozone.

5. Discussion

The advantage of comparing the results from the two GMI simulations is that there is a single difference between the simulations: the input meteorological fields. These meteorological fields were graded in SD2004 before use in the GMI CTM, and both reproduce many features of observations. Several aspects of the evaluation in SD2004 and the present comparisons with radical and reservoir species suggest that GMI_{FVGCM} will provide a more realistic assessment. These include the following:

1. The mixing ratio for total inorganic chlorine is larger in the lower and middle stratosphere in GMI_{FVGCM} than in GMI_{FVDAS}. This is consistent with the age of air produced by the two meteorological fields. The HCl column from GMI_{FVGCM} agrees better with observations than that from GMI_{FVDAS}. Note that mixing ratio boundary conditions for chlorine source gases guarantee nearly identical total inorganic chlorine in the upper stratosphere.
2. Total odd nitrogen from GMI_{FVGCM} is in better agreement with a lower stratospheric NO_y climatology [*Strahan, 1999*] than that simulated with GMI_{FVDAS}. This is consistent with somewhat better agreement for the annual mean HNO_3 column with that produced by GMI_{FVGCM}.

There are also deficiencies in the GMI_{FVGCM} simulation that will have a direct bearing on its predicted ozone change:

1. In the middle and upper stratosphere, NO_x mixing ratios are low compared with HALOE observations. This result is consistent with SD2004 comparison of simulated CH_4 with that observed by HALOE. As is the case for CH_4, there is too little transport of NO_x out of the tropical source region.
2. ClO from GMI_{FVGCM} is high compared with MLS ClO. The high ClO in GMI_{FVGCM} is accompanied by low HCl as a result of low CH_4 and thus low production of HCl.

Both the high ClO and the low NO_x are due to the insufficient transport out of the tropics in the middle and upper stratosphere. We emphasize that the high ClO is chemically unrelated to the low NO_x.

The good agreement with the diel dependence of $ClONO_2$ is found because $ClONO_2$ is not important at the pressure where ClO and the discrepancy between simulated and observed ClO are the largest. The deficiency in the daytime $ClONO_2$ and the faster than observed sunset rise in the $ClONO_2$ is common to both simulations. Similarly, the somewhat weaker than observed seasonal cycle in HNO_3 is common to both simulations. Comparisons of TOMS with simulated total column ozone are of similar quality.

This analysis suggests that the future upper stratospheric ozone in GMI_{FVGCM} will be more sensitive to chlorine decrease than GMI_{FVDAS} and also more sensitive than the actual atmosphere based on the MLS observations. The prediction will depend on other things not considered here – of obvious importance is the representation and propagation

of the ozone hole. These and other aspects of the two simulations of the 2030 atmosphere will be discussed in future work.

Acknowledgments: This work was funded by the NASA Atmospheric Chemistry, Modeling and Analysis Program. Part of this work was performed under the auspices of the U.S. Department of Energy by University of California Lawrence Livermore National Laboratory under contract No. W-7405-Eng-48.

Bibliography

Barath, F. T., et al., The Upper Atmosphere Research Satellite Microwave Limb Sounder Instrument, *J. Geophys. Res., 98,* 10,751-10,762, 1993.

Brühl, C. et al., Halogen Occultation Experiment ozone channel validation, *J. Geophys. Res., 101,* 10,217-10,240, 1996.

Brühl C., and P. J. Crutzen, NO_x-catalyzed ozone destruction and NO_x activation at midlatitudes to high latitudes as the main cause of the spring to fall ozone decline in the Northern Hemisphere, *J. Geophys. Res., 105*, 12,163-12,168, 2000.

Chapman, S., On Ozone and Atomic Oxygen in the Upper Atmosphere, *Phil. Mag. 10*, 369-383, 1930.

Considine D. B., A. R. Douglass, P. S. Connell, D. E. Kinnison, D. A Rotman, A polar stratospheric cloud parameterization for the global modeling initiative three-dimensional model and its response to stratospheric aircraft, *J. Geophys. Res., 105*, 3,955-3,973, 2000.

Considine, D. B., P. S. Connell, D. J. Bergmann, D. A. Rotman, S. E. Strahan, Sensitivity of Global Modeling Initiative CTM predictions of Antarctic ozone recovery to GCM and DAS generated meteorological fields, *submitted to J. Geophys. Res.*, 2004.

Douglass, A. R., M. J. Prather, T. M. Hall, S. E. Strahan, P. J. Rasch, L. C. Sparling, L. Coy, and J. M. Rodriguez, Choosing meteorological input for the global modeling initiative assessment of high-speed aircraft, *J. Geophys. Res., 104*, 27,545-27,564, 1999.

Dessler, A. E., et al., Correlated observations of HCl and $ClONO_2$ from UARS and implications for stratospheric chlorine partitioning, *Geophys. Res. Lett., 22*, 1721-1724, 1995.

Fahey, D. W., K. K. Kelly, G. V. Ferry, L. R. Poole, J. C. Wilson, D. M. Murphy, M. Loewenstein, K. R. Chan, In situ measurements of total reactive nitrogen, total water, and aerosol in a polar stratospheric cloud in the Antarctic, *J. Geophys. Res., 94* 11,299-11,315 1989.

Froidevaux L., J. W. Waters, W. G. Read, P. S. Connell, D. E. Kinnison, J. M. Russell Variations in the free chlorine content of the stratosphere (1991-1997): Anthropogenic, volcanic, and methane influences, *J. Geophy. Res. 105*, 4471-4481, 2000.

Gettelman, A., J. R. Holton, and A. R. Douglass, Simulations of water vapor in the lower stratosphere and upper troposphere, *J. Geophys. Res., 105*, 9003-9023, 2000.

Gordley, L. L., et al., Validation of nitric oxide and nitrogen dioxide measurements made by the Halogen Occultation Experiment for UARS platform, *J. Geophys. Res., 101*, 10,241-10,266, 1996

Gray L. J., J. M. Russell, Interannual variability of trace gases in the subtropical winter stratosphere, *J. Atmos. Sci., 56*, 977-993, 1999.

Jackman, C. H., A. R. Douglass, K. F. Brueske, S. A. Klein, The influence of dynamics on two-dimensional model results: simulations of ^{14}C and stratospheric aircraft NO_x injections, *J. Geophys. Res., 96,* 22,559-22,572, 1991.

Jacobson M. Z., Improvement of SMVGEAR II on vector and scalar machines through absolute error tolerance control, *Atmos. Env., 32*, 791-796, 1998.

Jöckel, P., R. V. Kuhlmann, M.G. Lawrence, B. Steil, C.A.M. Brenninkmeijer, P.J. Crutzen, P.J. Rasch, and B. Eaton, On a fundamental problem in implementing flux-form advection schemes for tracer transport in three-dimensional general circulation and chemical tracer models, *Q. J. R. Meteorol. Soc.*, *127*, 1035-1052, 2001.

Jet Propulsion laboratory (JPL), Chemical kinetics and photochemical data for use in stratospheric modeling, *Jet Propul. Lab. Pub. 00-3*, edited by S. P Sander et al., Jet Propulsion Laboratory, Pasadena, Calif., 2000.

Jet Propulsion Laboratory (JPL), Chemical Kinetics and photochemical data for use in atmospheric studies, *Jet. Propul. Lab. Pub 02-25*, edtied by S. P. Sander et al., Jet Propulsion Laboratory, Pasadena, Calif., 2003.

Kawa, S. R., et al., Assessment of the Effects of High-Speed Aircraft in the Stratopshere: 1998, NASA Technical Memorandum NASA/TP-1999-20937, NASA Goddard Space Flight Center, Greenbelt MD 20771, 1999.

Kiehl, J. R., J. J Hack, G. B. Bonan, B. A. Boville, D. L. Williamson, and P. J. Rasch, The national center for atmospheric research community climate model: CCM3, *J. Clim., 11,* 1131-1149, 1998.

Kinnison D. E., et al., The Global Modeling Initiative assessment model: Application to high-speed civil transport perturbation, *J. Geophy. Res., 106,* 1693-1711, 2001.

Koike, M., N. B. Jones, W. A. Matthews, P. V. Johnston, R. L. McKenzie, D. Kinnison, and J. Rodriguez, Impact of Pinatubo aerosols on the partitioning between NO_2 and HNO_3, *Geophys. Res. Lett., 21*, 597-600, 1994.

Kumer J. B., S. R. Kawa, A. E. Roche, J. L. Mergenthaler, S. E. Smith, F. W. Taylor, P. S. Connell, A. R. Douglass, UARS first global N_2O_5 data sets: Application to a stratospheric warming event in January 1992, *J. Geophys. Res., 102*, 3575-3582, 1997.

Livesey N. J., W. G. Read, L. Froidevaux, J. W. Waters, M. L. Santee, H. C. Pumphrey, D. L. Wu, Z. Shippony, R. F. Jarnot, The UARS microwave limb sounder version 5 data set: Theory, characterization, and validation, *J. Geophys. Res., 108,* 4378, do:10.1029/2002JD002273, 2003.

Lin, S.-J., A finite-volume integration scheme for computing pressure-gradient forces in general vertical coordinates, *Q. J. R. Meteorol. Soc., 123,* 1749-1762, 1997.

Lin, S.-J., and R. B. Rood, Multidimensional flux form semi-Lagrangian transport schemes, *Mon. Wea. Rev., 124,* 2046-2070, 1996.

Lin, S.-J., and R. B. rood, An explicit flux-form semi-Lagrangian shallow-water model on the sphere, *Q. J. R. Meteorol. Soc., 124*, 2477-2498, 1997.

McPeters, R. D., et al., Earth Probe Total Ozone Mapping Spectrometer (TOMS) Data Products User's Guide, NASA Reference Publication: Goddard Space Flight Center, Greenbelt MD 20771, 1998.

Mergenthaler J. L., et al., Validation of CLAES ClONO2 measurements, *J. Geophys. Res., 101*, 9603-9620, 1996.

Nevison, C. D., S. Solomon, and R. R. Garcia, Model overestimates of NO_y in the upper stratosphere, *Geophys. Res. Lett., 24,* 803-806, 1997.

Newman, P. A., D. W. Fahey, W. H. Brune, M. J. Kurylo, Photochemistry of Ozone Loss in the Arctic Region in Summer (POLARIS) CACGP/IGAC 1998

Symposium (CACGP/IGAC) – Preface, *J. Geophys. Res., 104*, 26,481-26,496, 1999.

Newman P. A., et al., An overview of the SOLVE/THESEO 2000 campaign, *J. Geophys. Res., 107*, 9259, 2002.

Pan, L. W. L., E. J. Hintsa, E. M. Stone, E. M. Weinstock, W. J. Randel, The seasonal cycle of water vapor and saturation vapor mixing ratio in the extratropical lowermost stratosphere, *J. Geophys. Res., 105*, 26,519-26,530, 2000.

Plumb, R. A. and M. K. W. Ko, Interrelationships between mixing ratios of long lived stratospheric constituents, *J. Geophys. Res., 97*, 10,145-10,156, 1992.

Prather, M., M. McElroy, S. Wofsy, G. Russell, and D. Rind, Chemistry of the global troposphere: Fluorocarbons as tracers of air motion, *J. Geophys. Res., 92*, 6579-6613, 1987.

Randel, W. J., Seasonal evolution of planetary waves in the southern hemisphere stratosphere and troposphere, *Q. J. R. Meteorol. Soc., 114*, 1385-1409, 1988.

Randel W. J., F. Wu, J. M. Russell, A. Roche, J. W. Waters, Seasonal cycles and QBO variations in stratospheric CH_4 and H_2O observed in UARS HALOE data, *J. Atmos. Sci., 55*, 163-185, 1998.

Ray, E. A., F. L. Moore, J. W. Elkins, G. S. Dutton, D. W. Fahey, H. Vomel, S. J. Oltmans, and K. H. Rosenlof, Transport into the Northern Hemisphere lowermost stratosphere revealed by in situ tracer measurements, J. *Geophys. Res., 104*, 26,565-26,580, 1999.

Rinsland, C. P., et al., Long-term trends of inorganic chlorine from ground-based infrared solar spectra: Past increases and evidence for stabilization, 4252,

doi:10.1029/2002JD003001, 2003(a).

Rinsland, C. P., D. K. Weisenstein, M. K. W. Ko, C. J. Scott, L. S. Chiou, E. Mahieu, R. Zander, and P. Demoulin, "Post-Mount Pinatubo eruption ground-based stratospheric column measurements of HNO3, NO, and NO2 and their comparison with model calculation", *J. Geophys. Res., 108*, 4437, doi:10.1029/2002JD002965, 2003(b).

Roche, A. E., J. B. Kumer, J. L. Mergenthaler, G. A. Ely, W. G. Uplinger, J. F. Potter, T. C. James and L. W. Sterritt, The Cryogenic Limb Array Etalon Spectrometer, (CLAES) on UARS: Experiment description and performance, *J. Geophys. Res., 98*, 10,763-10,775, 1993.

Rood, R. B., A. R. Douglass, M. C. Cerniglia, L. C. Sparling and J. E. Nielsen, Seasonal variability of middle-latitude ozone in the lowermost stratosphere derived from probability distribution functions, *J. Geophys. Res., 105*, 17,793-17,805, 2000.

Rotman D. A., et al., Global Modeling Initiative assessment model: Model description, integration, and testing of the transport shell, *J. Geophys. Res., 106*, 1669-1691, 2001.

Russell, J. M., III, L L. Gordley, J. H. Park, S. R. Drayson, A. F. Tuck, J. E. Harries, R. J. Cicerone, P. J. Crutzen and J. E. Frederick, The Halogen Occultation Experiment, *J. Geophys. Res., 98,* 10,777-10,797, *1993.*

Russell, J. M. III, et al., Validation of hydrogen chloride measurements made by the Halogen Occultation Experiment from the UARS Platform, *J. Geophys. Res., 101*, 10,151-10,162, 1996.

Schneider, M., T. Blumenstock, F. Hase, M. H. Föpfner, E. Cuevas, A. Redondas, J. M.

Sancho, "Ozone Profiles and Total Column Amounts derived at Ivana, Tenerife Island from FTIR Solar Absorption Spectra, and its Validation by an Intercomparison to ECC-Sonde and Brewer Spectrometer Measurements, *submitted to J. Quant. Spect. Rad. Trans.*, 2003.

Sen B., G. C. Toon, G. B. Osterman, J.-F. Blavier, J. J. Margitan and R. J. Salawitch, and G. K. Yue, Measurements of reactive nitrogen in the stratosphere, *J. Geophys. Res., 103*, 3571-3585, 1998.

Strahan, S. E., M. Loewenstein, J. R. Podolske, Climatology and small-scale structure of lower stratospheric N2O based on in situ observations, *J. Geophys. Res.*, 2195-2208, 1999.

Strahan, S. E., Climatologies of lower stratospheric NO_y and O_3 and correlations with N_2O based on in situ observations, *J. Geophys. Res., 104*, 30,463-30,480, 1999.

Strahan, S. E., Influence of planetary wave transport on Arctic ozone as observed by Polar Ozone and Aerosol Measurement (POAM) III, *J. Geophys. Res., 107*, 4417, 2002.

Strahan, S. E., and A. R. Douglass, Evaluating the credibility of transport processes in the Global Modeling Initiative 3D model simulations of ozone recovery, *J. Geophys. Res., in press*, 2004.

Toon, G. C., The JPL MkIV interferometer, *Opt. Photonics News, 2*, 19-21, 1991.

Waters, J. W., et al., Validation of UARS Microwave Limb Sounder ClO measurements, *J. Geophys. Res., 101,* 10091-10,127, 1996.

Wofsy, S. C., R. C. Cohen, A. L. Schmeltekopf, Overview: The Stratospheric Photochemistry Aerosols and Dynamics Expedition (SPADE) and Airborne

Arctic Stratospheric Expedition II (AASE II), *Geophys. Res. Lett., 21* 2535-2538 1994.

WMO, Scientific Assessment of Ozone Depletion: 2002, World Meteorological Organization Global Ozone Research and Monitoring Project, Report No. 47, 2003.

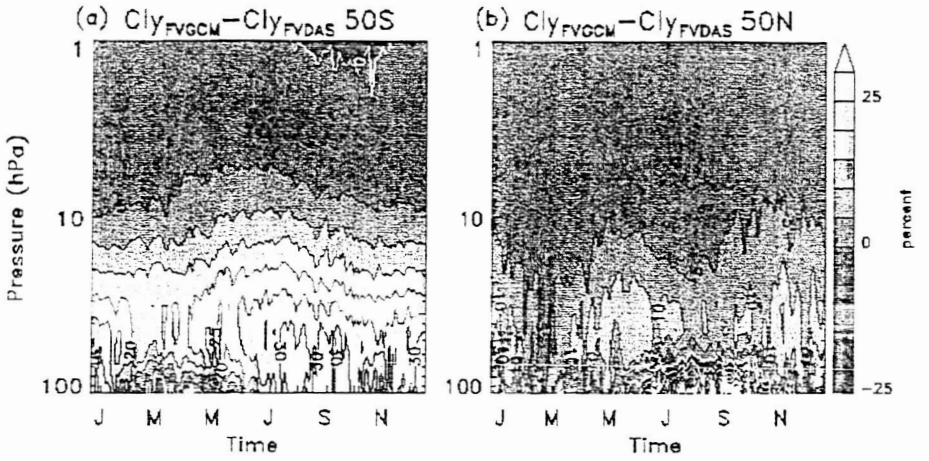

Figure 1(a) The seasonal cycles of the difference $Cly_{FVGCM} - Cly_{FVDAS}$ at 50°S; (b) same as (a) but 50°N.

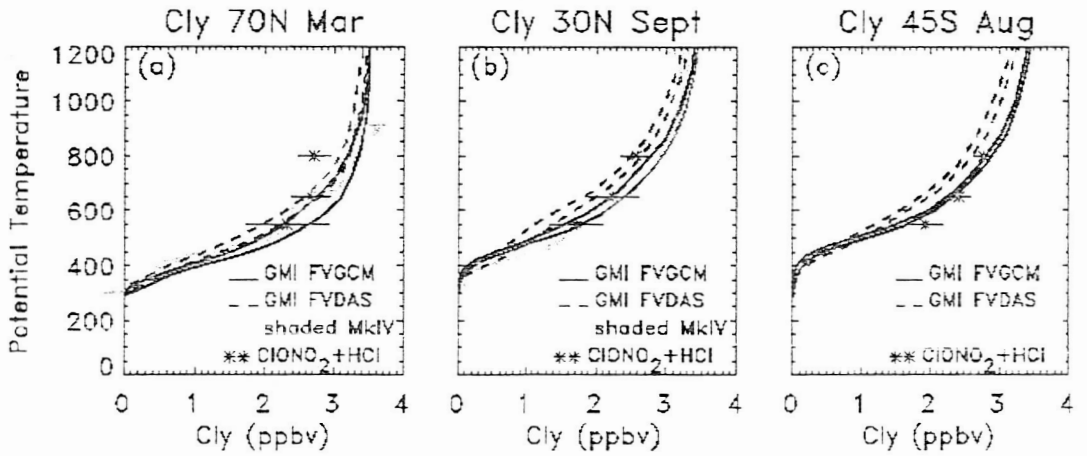

Figure 2 (a) The shaded profile indicates Cl_y ± error from MkIV measurements of chlorine containing species at 70°N. The lines are the model zonal mean profiles ± one-sigma. Cl_y estimates from HALOE HCl + CLAES $ClONO_2$ are shown by stars. The horizontal lines show the one-sigma range of the HALOE plus CLAES estimate. (b) Same as (a) but for 30°N. (c) Model profiles as in (a) compared with the HALOE HCl plus CLAES $ClONO_2$ estimate. See text for discussion.

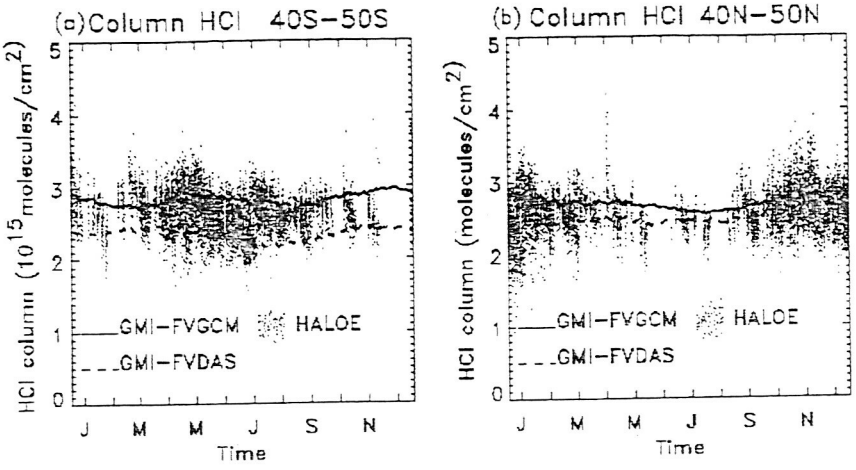

Figure 3(a) HCl column 100 – 1 hPa calculated from HALOE profiles between 40°S-50°S for 1993 – 2000 (dots) from GMI_{FVGCM} and GMI_{FVDAS} profiles at 46°S for 1995; (b) same as (a) for HALOE profiles between 40°N and 50°N and simulated profiles at 46°N.

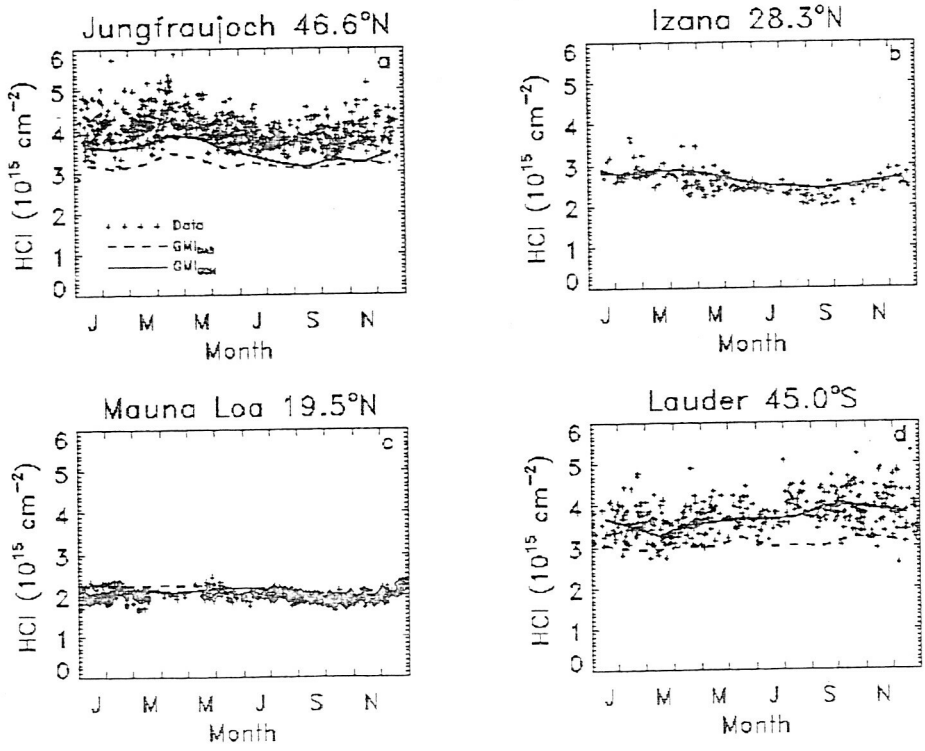

Figure 4. Measured column amounts of HCl at four NDSC sites compared to GMI model calculations. (a) Jungfraujoch; (b) Izana; (c) Mauna Loa; (d) Lauder

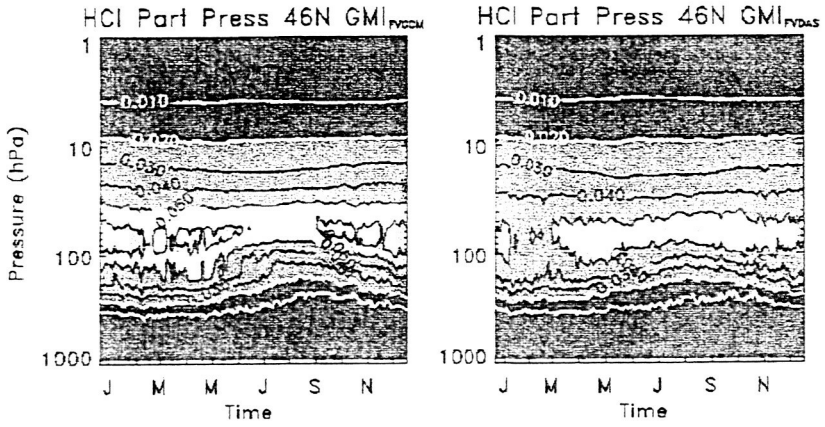

Figure 5(a) Partial pressure of HCl (nanobars) at 46 N from GMI_{FVGCM} (b) same as (a) for GMI_{FVDAS}

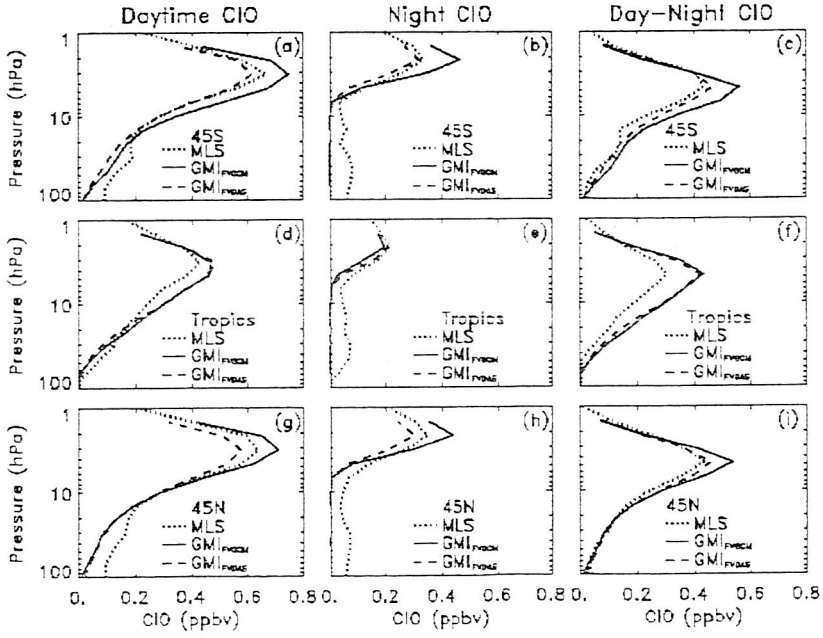

Figure 6 Annually averaged MLS ClO is compared with that from the two simulations. Each row corresponds to a latitude; the data are averages of all observations within 10 degrees of the latitude specified on the figure. The columns correspond to daytime measurements (left), nighttime measurements (center) and the day-night difference

(right). Measurements bias is eliminated from the comparisons by using the day-night difference.

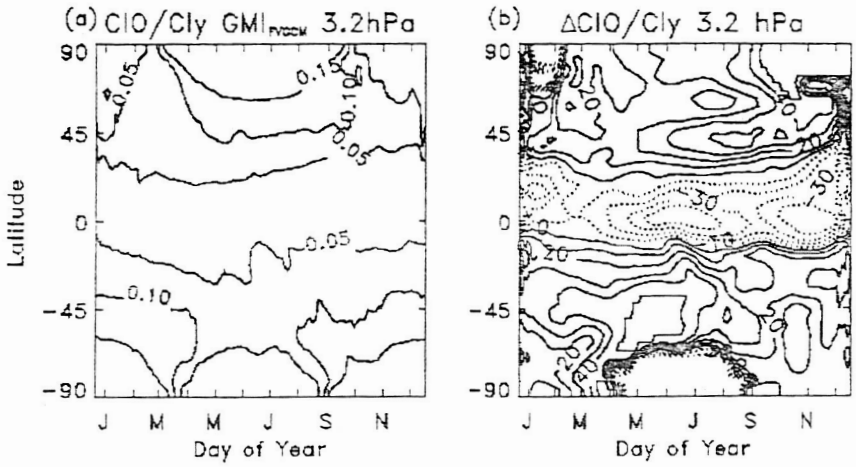

Figure 7(a) The ratio for daytime ClO/Cly from GMI_{FVGCM}; (b) The percentage difference in the ClO/Cly ratio between GMI_{FVGCM} and GMI_{FVDAS}. This ratio is up to 50% higher in GMI_{FVGCM} outside the tropics.

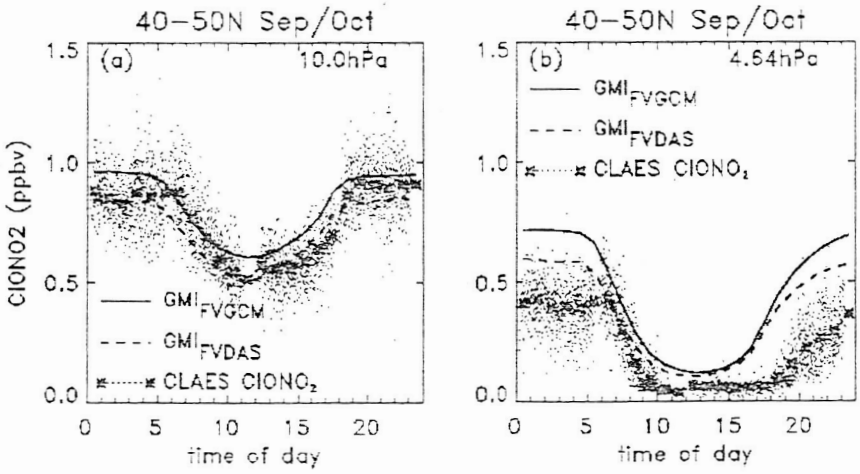

Figure 8 (a) 10 hPa CLAES $ClONO_2$ observed between Sept. 21, 1992 - Oct. 29, 1992 for the 40°N-50°N are shown at the local time for measurements and for the simulations; (b) Same as (a) except for 4.64 hPa.

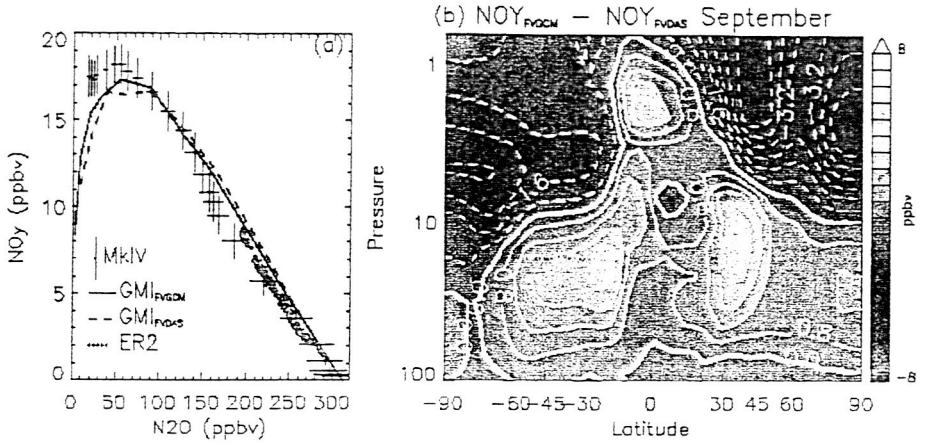

Figure 9 (a) NO_y vs. N_2O correlations for MkIV measurements at 35N in September 1993 (crosses) and ER-2 data at 25N-35N February 1992 (dots). Simulated values are shown for 35N September. (b) The difference in zonal mean NO_y for the two simulations.

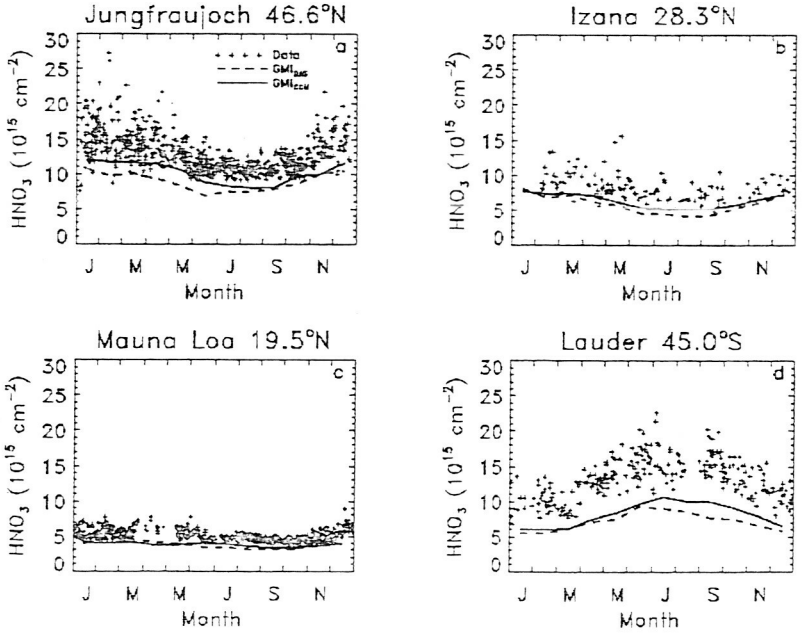

Figure 10 Measured column amounts of HNO_3 at four NDSC sites compared to GMI model calculations. (a) Jungfraujoch; (b) Izana; (c) Mauna Loa; (d) Lauder.

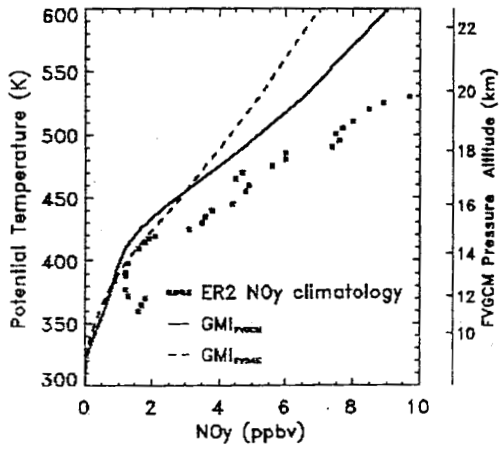

Figure 11. Lower stratospheric NO_y from the two simulations compared with a climatology developed from ER2 measurements [*Strahan*, 1999] for June at 45°N.

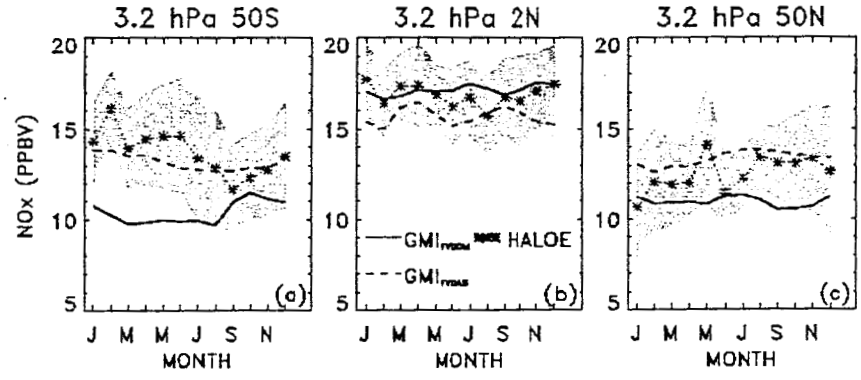

Figure 12 (a) Sunset HALOE NO + NO_2 at 3.2 hPa (stars) compared with NO_x=NO+NO_2+N_2O_5 from both simulations. HALOE data for 40°S - 60°S, 1993-2000, are sorted by month. The shaded area is the 1 standard deviation difference from the mean of the HALOE observations. (b) same as (a) but for 10°S–10°N; (c) same as (a) but for 40°N – 60°N.

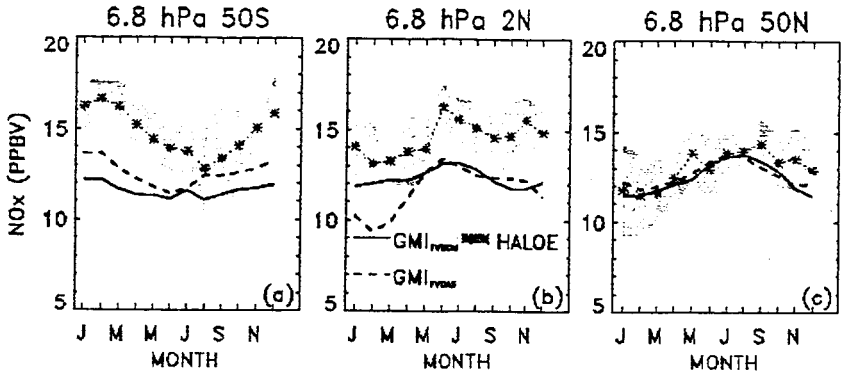

Figure 13 (a) Sunset HALOE NO + NO_2 at 6.8 hPa (stars) compared with simulated NO_x=NO+NO_2+N_2O_5. HALOE data for 40°S - 60°S, 1993-2000, are sorted by month. The shaded area is the 1 standard deviation difference from the mean of the HALOE observations. (b) same as (a) but for 10°S – 10°N; (c) same as (a) but for 40°N – 60°N.

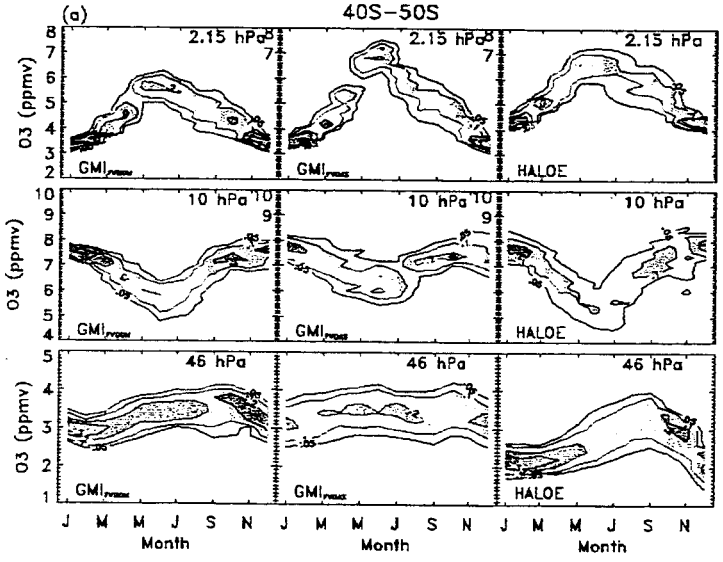

Figure 14(a) Contours of ozone probability distributions from the GMI_{FVGCM} (left column), GMI_{FVDAS} (center column), and HALOE (right column) at 2.15 hPa (top row); 10 hPa (center row) and 46 hPa (bottom row) for southern middle latitudes (40°S-50°S). Contours greater than 0.1 are shaded, with darker contours indicating higher probability.

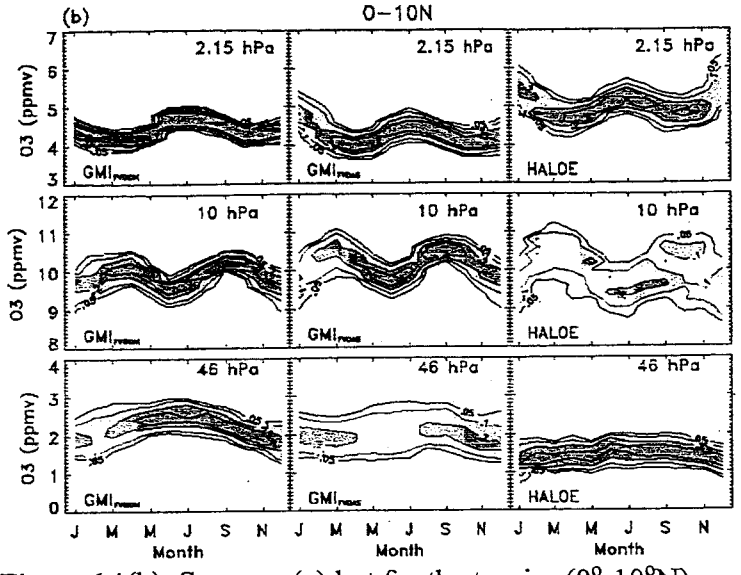

Figure 14(b) Same as (a) but for the tropics (0°-10°N)

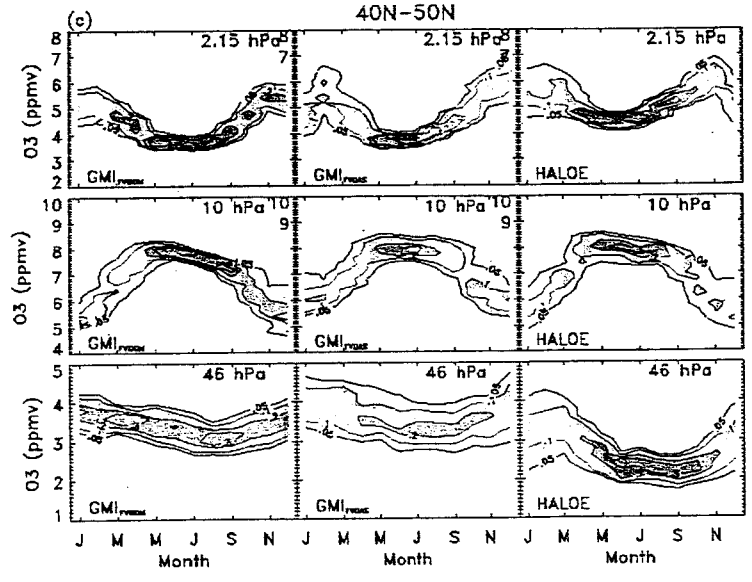

Figure 14(c) Same as 14(a) but for northern middle latitudes (40°N-50°N).

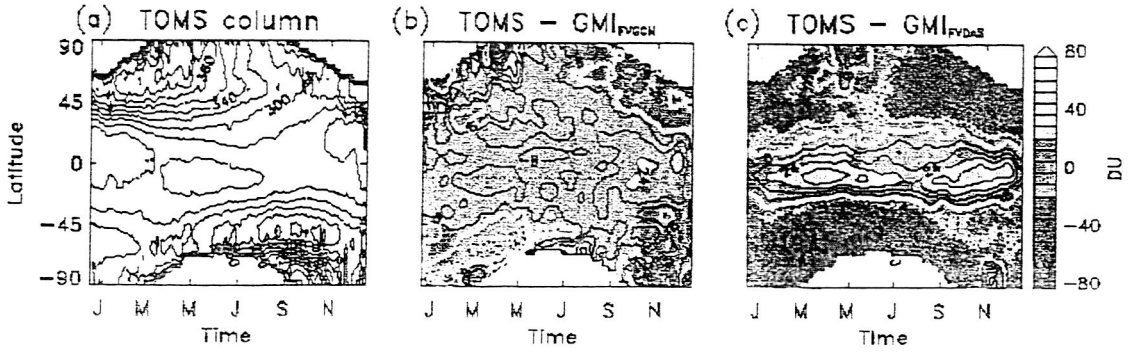

Figure 15 (a) TOMS zonal mean total ozone for 1994-1998; (b) The difference between TOMS and GMI_{FVGCM} zonal mean columns; the white bold white contour is the zero line; solid (dashed) contours indicate that the simulated columns are smaller than (greater than) TOMS; (c) same as (b) for GMI_{FVDAS}.

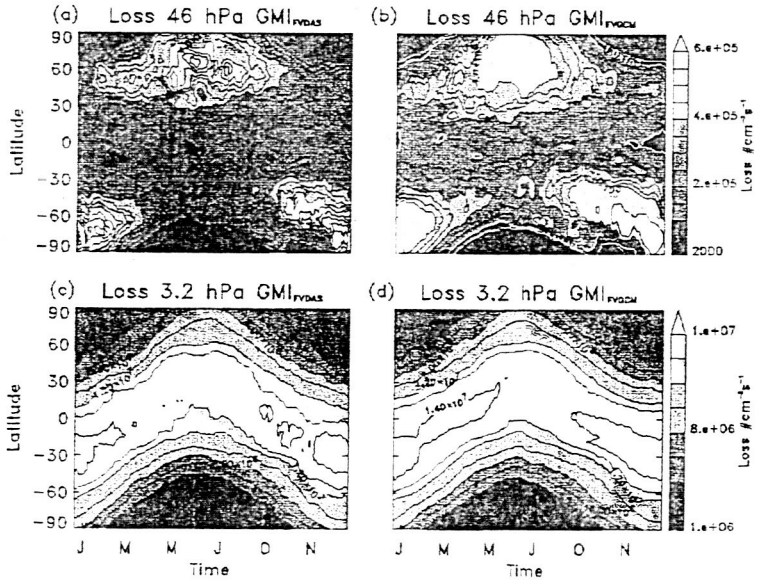

Figure 16(a) total loss from GMI_{FVDAS} at 46 hPa; (b) same as (a) but for GMI_{FVGCM}; (c) same as (a) but for 3.2 hPa; (d) same as (b) but for 3.2 hPa.

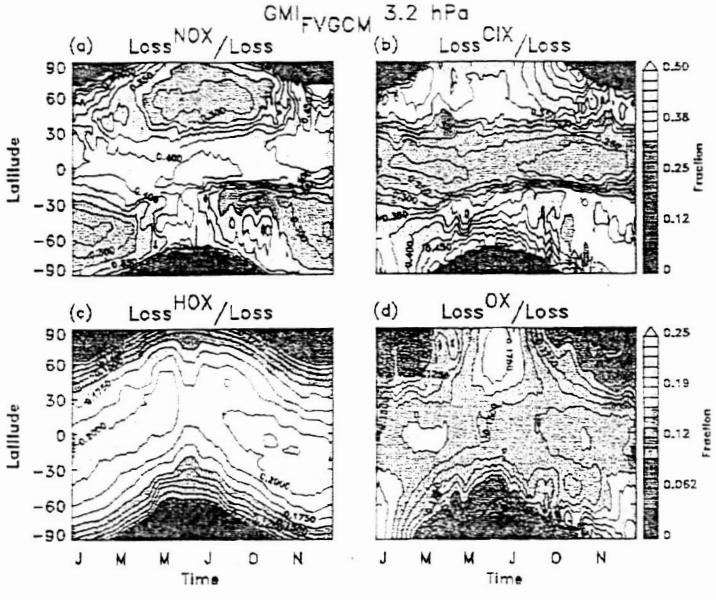

Figure 17 (a) Fraction of ozone loss due to reactions with NO_x species (b) Fraction of ozone loss due to reactions with chlorine species; (c) fraction of ozone loss due to reactions with hydrogen species; (d) fraction of ozone loss due to the reaction of atomic oxygen with ozone. All are calculated using results from GMI_{FVGCM}; all fields are smoothed for clarity of presentation.

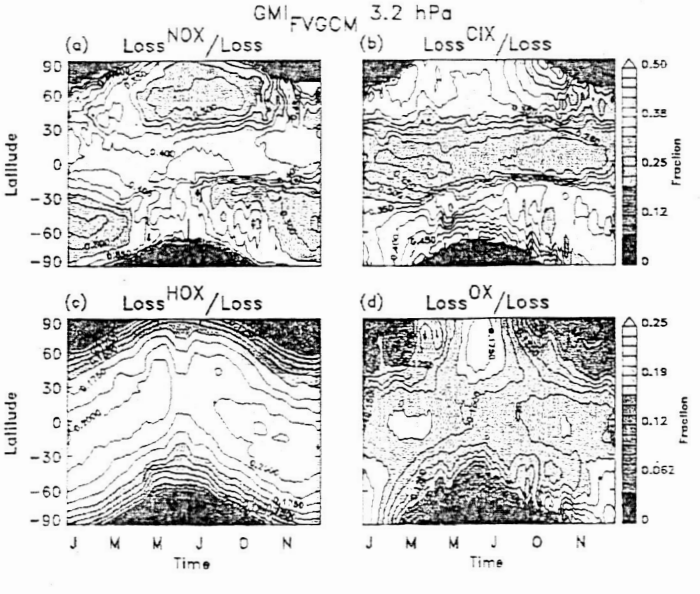

Figure 18 Same as Figure 17 using simulation results from GMI_{FVDAS}.